

# In situ TEM observation of neck formation during oriented attachment of PbSe nanocrystals

Yu Wang<sup>1,2</sup>, Xinxing Peng<sup>1,3</sup>, Alex Abelson<sup>4</sup>, Bing-Kai Zhang<sup>1</sup>, Caroline Qian<sup>4</sup>, Peter Ercius<sup>5</sup>, Lin-Wang Wang<sup>1</sup>, Matt Law<sup>4</sup>, and Haimei Zheng<sup>1,2</sup> (✉)

<sup>1</sup> Materials Sciences Division, Lawrence Berkeley National Laboratory, Berkeley, California 94720, USA

<sup>2</sup> Department of Materials Science and Engineering, University of California, Berkeley, California 94720, USA

<sup>3</sup> State Key Lab of Physical Chemistry of Solid Surfaces, Collaborative Innovation Center of Chemistry for Energy Materials, College of Chemistry and Chemical Engineering, Xiamen University, Xiamen 361005, China

<sup>4</sup> Department of Chemistry, University of California, Irvine, California 92697, USA

<sup>5</sup> National Center for Electron Microscopy, Molecular Foundry, Lawrence Berkeley National Laboratory, Berkeley, California 94720, USA

© Tsinghua University Press and Springer-Verlag GmbH Germany, part of Springer Nature 2019

Received: 16 May 2019 / Revised: 11 July 2019 / Accepted: 16 July 2019

## ABSTRACT

Oriented attachment of nanocrystals is an important route to constructing epitaxially-connected nanocrystal superlattices for various applications. During oriented attachment of semiconductor nanocrystals, neck can be formed between nanocrystals and it strongly influences the properties of the resulting superlattice. However, the neck formation mechanism is poorly understood. Here, we use *in situ* liquid cell transmission electron microscopy to directly observe the initiation and growth of homoepitaxial necks between PbSe nanocrystals with atomic details. We find that neck initiation occurs slowly (~ 10 s) when two nanocrystals approach to each other within an edge-to-edge distance of 0.6 nm. During neck initiation, Pb and Se atoms diffuse from other facets into the gap, forming “dynamic reversible” filaments. Once the filament (neck) width is larger than a critical size of 0.9 nm, it gradually (15 s) widens into a 3-nm-wide neck. The atomic structure of the neck is further obtained using *ex situ* aberration-corrected scanning TEM imaging. Neck initiation and growth mechanisms are elucidated with density functional theory calculations. Our direct unveiling of the atomic pathways of neck formation during oriented attachment shed light into the fabrication of nanocrystal superlattices with improved structural order and electronic properties.

## KEYWORDS

PbSe nanocrystals, quantum dots, superlattices, necking, oriented attachment, liquid cell transmission electron microscopy (TEM)

## 1 Introduction

Oriented attachment of colloidal nanocrystals occurs in a variety of natural and synthetic systems [1, 2], in which nanocrystals connect preferentially along specific crystal facets to form a single crystal. During oriented attachment, the inter-nanocrystal connection, which is achieved through a “necking” process [3–6], is essential for regulating the coherent coupling effects in superlattices [7, 8] and thus enabling the emergence of various novel properties [7, 9, 10]. For instance, epitaxially-connected superlattices of semiconductor nanocrystals may show remarkable electronic phenomena including topological states and Dirac cones [11–13]. These phenomena will be favored in superlattices with atomically-uniform inter-nanocrystal necks that increase the electron delocalization length [14, 15]. To understand necking in nanocrystal superlattices, recent efforts have used X-ray scattering [16–18] and *ex situ* TEM [19–21] to characterize the superlattice structure before and after oriented attachment. These measurements indicate that the center-to-center distance of epitaxially-connected nanocrystals is often larger than the diameter of the initial nanocrystals [12, 22]. It has been presumed that necking may be achieved through a “click and cascade” model when two nanocrystals are at a short range and separated by solvent molecules [22]. However, the mechanism of neck formation in nanocrystal

superlattices is unclear due to the lack of direct observation [23–26]. Elucidating the mechanism(s) of nanocrystal necking is significant not only for interpreting semiconductor crystallization through particle attachment [27], but also for improving the inter-nanocrystal connectivity in nanocrystal superlattices to achieve novel electronic properties [14, 28].

Here, we report real-time atomic-resolution imaging of the necking process during oriented attachment of PbSe nanocrystals by liquid-phase TEM [29–32]. During the superlattice transformation from quasi-hexagonal oleate-capped PbSe nanocrystal monolayers to quasi-square epitaxially-connected nanocrystal monolayers, we find that the necking occurs in three stages: (i) nanocrystals first approach each other and the lattice angle changes from ~ 60° to ~ 90°, indicating a geometry change from hexagonal to square; (ii) when the neighboring nanocrystals reach a gap (surface-to-surface) distance of ~ 0.6 nm due to the separation of ligand residuals, they stop moving and start building a neck. Atom-resolved imaging shows that it takes 5–10 s to form a stable neck nucleus with a critical size of 0.6 nm × 0.9 nm (neck length and width); (iii) after initiation, the neck grows to 3 nm in width in ~15 s. Using *ex situ* scanning TEM, we confirm the formation of two-atom-long necks during the superlattice phase transition. The mechanism of neck initiation and growth is rationalized with density functional theory (DFT) calculations.

## 2 Results and discussion

We formed hexagonal self-assembled monolayers of oleate-capped PbSe nanocrystals (6.2 nm diameter) by drop-casting 4  $\mu\text{L}$  of a 0.5 mg/mL hexane suspension of the nanocrystals onto a 10-nm thick carbon-film TEM grid. We then deposited 100 nL of anhydrous ethylene glycol (EG) on a second TEM grid and sandwiched the two grids together to form a carbon-film liquid cell for *in situ* TEM imaging. The fluctuation of EG during *in situ* imaging initiates the oriented attachment of PbSe nanocrystals, enabling real-time imaging of the necking process with atomic resolution (Movies ESM1–ESM4).

The image series in Fig. 1(a) and Movie ESM1 depict the oriented attachment of six nanocrystals (1 to 6). At 0 s, nanocrystals 2 and 3 are already connected, whereas the other nanocrystals are discrete in a quasi-hexagonal geometry. Over the next 50 s, the nanocrystals move towards their neighboring nanocrystals and fuse into a quasi-square superlattice. The trajectory of each nanocrystal center and the inter-nanocrystal connectivity are shown in Fig. 1(b), from which we analyze the change of four representative lattice angles ( $\alpha$ – $\delta$ ). As shown in Fig. 1(c), all four lattice angles increase from  $\sim 60^\circ$  towards  $90^\circ$ , indicating the superlattice symmetry changes from hexagonal to square as the nanocrystals approach each other.

The change of gap distances (distance between the nanocrystal surfaces) between five initially unconnected nanocrystal pairs is plotted in Fig. 1(d). Nanocrystals 1 and 2 (a representative pair) approach each other from a gap distance of 4.5 nm at 0 s with a speed of  $\sim 0.3$  nm/s. The approach speed gradually decreases and translational motion stops at a distance of 0.6 nm at 21 s. As shown in the third image in Fig. 1(a) (20.0 s), there is still a clear gap between nanocrystals 1 and 2 at this time.

It takes an additional  $\sim 10$  s to build a discernible neck, which we consider the onset of neck initiation. Although other nanocrystal pairs have different initial gap distances and different approach speeds, all nanocrystal pairs were observed to follow the same three-stage oriented attachment process (Fig. 1(d)): (i) the nanocrystals move to within  $\sim 0.6$  nm of each other, (ii) a neck nucleus forms after 5–10 s, and (iii) the neck widens until it becomes a stable size. Additional examples of this three-stage oriented attachment process can be found in Movies ESM2 and ESM3, which are analyzed in

Figs. S1 and S2 in the Electronic Supplementary Material (ESM) and show a very similar final gap distance ( $\sim 0.6$  nm) and neck initiation time (5–10 s).

The atomistic pathway of neck initiation and growth is explored in Movie ESM4 and Fig. 2(a). The clear lattice fringes visible throughout the movie enable us to reconstruct atomic models of neck initiation and growth (right column in Fig. 2(a)). We find that nanocrystals align in a same  $\langle 100 \rangle$  axial occurs before neck initiation. In the first image (2.0 s), the two unconnected nanocrystals are separated by 0.6 nm and show biaxially-aligned  $\{200\}$  planes perpendicular to the inter-nanocrystal axis. The  $d$ -spacing of the  $\{200\}$  planes remains constant at  $\sim 3.1$  Å during neck formation, indicating the absence of strong lattice distortion. By counting the  $\{200\}$  planes, we find that both nanocrystals initially have 20 atomic layers along the inter-nanocrystal direction, and after the oriented attachment, two extra  $\{200\}$  layers form in the 0.6 nm gap. As reflected by the edge trajectories of nanocrystals (Fig. 2(b)), the nanocrystal centers barely change position during the necking process, whereas the nanocrystal width (perpendicular to inter-nanocrystal direction) decreases slightly as the neck grows. This suggests that the necks grow as surface atoms on the lateral facets of the nanocrystals diffuse into the inter-nanocrystal regions. Note that, there is a slight increase in the length of the left nanocrystal in Fig. 2(b) during the later stage of neck growth, which is probably caused by the deformability of PbSe nanocrystals after the removal of capped ligands. Recently, we have reported that the deformability of PbSe nanocrystals is strongly dependent on the kinetics of ligand removal [33], e.g., fast ligand removal by ethylenediamine solution induces drastic elongation of nanocrystals along inter-nanocrystal direction, whereas slow ligand removal by EG (same condition used in the current work) leads to reduced deformability of nanocrystals. The driving force of nanocrystal deformation is ascribed to the dipole interaction between nanocrystals based on comparison experiments and molecular dynamics simulations [20, 33, 34]. Closer scrutiny of the *in situ* movies reveals that neck initiation involves the formation of transient atomic PbSe filaments (e.g., see image at 3.0 s) prior to the appearance of a stable neck nucleus. Figure 2(c) shows a time trace of the filament/neck width. We find that the width fluctuates between 0–0.9 nm from 2 to 7 s due to the formation and cleavage of thin PbSe filaments. Eventually, a

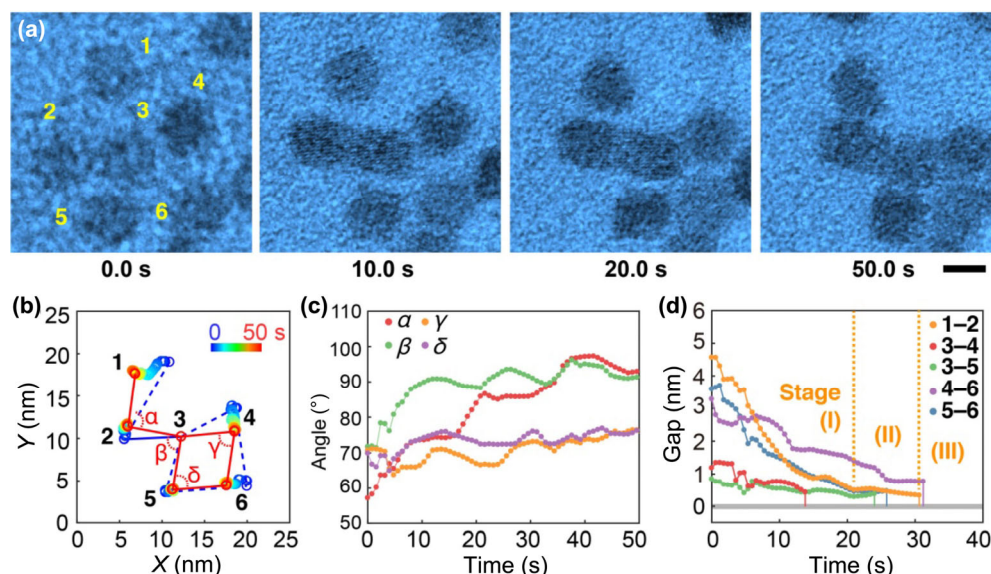


**Figure 1** Neck formation between PbSe nanocrystals during the transformation from an oleate-capped hexagonal to connected square assembly. (a) Sequence of *in situ* TEM images showing the translational motion and necking of six nanocrystals. Images are extracted from Movie ESM1 and shown in false color. Scale bar, 5 nm. (b) Trajectories of the nanocrystal centers showing the transformation from the hexagonal to square geometry. Dashed and solid lines denote nanocrystal pairs that are unconnected or connected, respectively. Four inter-nanocrystal angles are labeled  $\alpha$ – $\delta$ . (c) Plot of the four angles versus time. (d) Time trace of the gap distances of six nanocrystal pairs showing the three-stage necking pathway. Pair 1–2 (orange dots and lines) highlights the three stages of neck formation: (I) approach, (II) arrest and neck initiation, and (III) neck growth. When the trace falls to the gray bar (0 nm), it denotes a stable nucleus formed between the nanocrystal pair.

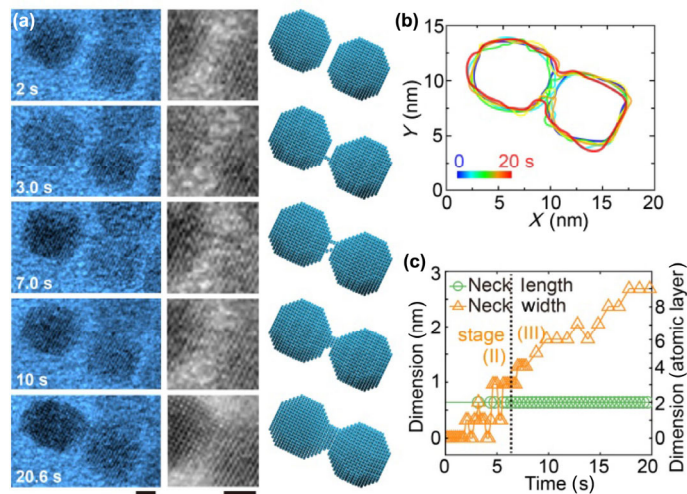


**Figure 2** Atomistic pathway of neck initiation between two PbSe nanocrystals. (a) Representative sequence of *in situ* TEM images (left column) extracted from Movie ESM4, magnified views (middle column) and atomic models (right column) showing the necking details. Only Pb atoms are shown in models for clarity and a closer comparison to TEM images. Both scale bars are 2 nm. (b) Trajectories of the nanocrystal edges showing the nanocrystal shape change during neck formation. (c) Time trace of the neck length and width during the neck initiation and growth stages (separated by dashed vertical line).

stable nucleus with a width of  $> 0.9$  nm forms and grows to  $\sim 2.7$  nm in width in 20 s. Meanwhile, the neck length is fixed at 0.6 nm (the final gap distance).

We employed *ex situ* high-angle annular dark field scanning TEM (HAADF-STEM) imaging to investigate neck formation in large-area superlattices. We performed the superlattice transformation with a similar procedure to the one used *in situ*, i.e., first forming a hexagonal monolayer on a carbon-film TEM grid, then immersing the grid in anhydrous EG for 30 s to trigger the oriented attachment. The large-area structures are characterized before and after EG treatment by HAADF-STEM and analyzed using custom computer vision scripts (Figs. 3(a)–3(e) and Fig. S3 in the ESM). We observe that nanocrystals are mostly epitaxially connected in the square superlattice (Fig. S4 in the ESM) and the center-to-center distance of adjacent nanocrystals is larger than the initial nanocrystal diameter, in accord with our *in situ* results and previous reports of square superlattices prepared by nanocrystal self-assembly on the surface of EG [12, 33]. We note that the precise neck length should not be directly calculated as the difference between center-to-center distance and nanocrystal diameter; instead, it should be calculated as difference between center-to-center distance and the nanocrystal size along  $\langle 100 \rangle$  directions. A precondition for obtaining monodisperse necks is the use of monodisperse nanocrystals. Statistical analysis of several images shows that nanocrystals in the hexagonal monolayer are highly monodisperse, with 95% of the nanocrystals having a diameter of  $6.2 \pm 0.1$  nm (Figs. 3(a) and 3(c)). These nanocrystals contain 20 atomic layers in the  $\langle 100 \rangle$  directions, which is consistent with the nanocrystal size measured in Fig. 2. After EG treatment, a square superlattice forms (Fig. 3(b)) with an average center-to-center distance of 6.7 nm (Fig. 3(d)). Therefore, the neck length is calculated as the difference between the center-to-center distance (6.7 nm) and the nanocrystal size along the  $\langle 100 \rangle$  directions (20 atomic layers, 6.1 nm). In addition, Fig. 3(e) shows the histogram of neck width, indicating an average width of 3.0 nm, comparable to the neck width measured *in situ* at 20 s (Fig. 2).

We confirmed an average neck length of two atomic layers by *ex situ* atomic-resolution imaging (Figs. 3(f) and 3(g)). The associated fast Fourier transform (FFT, Fig. 3(f) inset) shows the uniform oriented attachment in the connected superlattice. The overlaid boxes with a size of  $20 \times 20$  atomic layers help to visualize the necks and determine

their length (Fig. 3(g)). Most of the necks are two atomic layers long (Fig. 3(h)).

Previous studies on gold crystallization found that oriented attachment of gold nanocrystals may also involve the necking of nanoparticles with a gap distance of  $\sim 0.5$  nm [35, 36]. It was proposed that the gold nanocrystals stop at the small gap distance because of the separation of solvent, i.e., water [37]. Our recent atomic-resolution *in situ* TEM study on gold nanocrystals suggests the ligands could play an important role in separating gold nanocrystals during oriented attachment [38]. We have observed that the approaching PbSe nanocrystals stop at a gap distance of 0.6 nm before the neck initiation in EG, and we speculate that this is resulted from the ligand-enforced separation of nanocrystals. Because the EG treatment is not good at removing oleate ligands as other strong ligand-removal agents such as ethylenediamine (EDA) [39]. Most of the oleate remains bound after EG treatment, but the  $\{100\}$  facets have a much lower oleate coverage than the other facets since the binding energy is low. The residual bound oleate can move and flex and might be compressed to lie along the  $\{100\}$  surface, which stops the dots at  $\sim 0.6$  nm. As the atoms begin filling in the gap, they displace the oleate ligands, pushing the ligands out to the periphery of the neck or onto the other facets.

We performed a comparison experiment on the oriented attachment of PbSe nanocrystals in the presence of strong ligand-removal agent EDA, and found that when the oleate ligands were aggressively removed by EDA, the nanocrystals attached directly without showing the separation stage (Movie ESM5 and Fig. S5 in the ESM). This suggests that the separation of nanocrystals before neck initiation is more likely caused by oleate ligands rather than EG solvents.

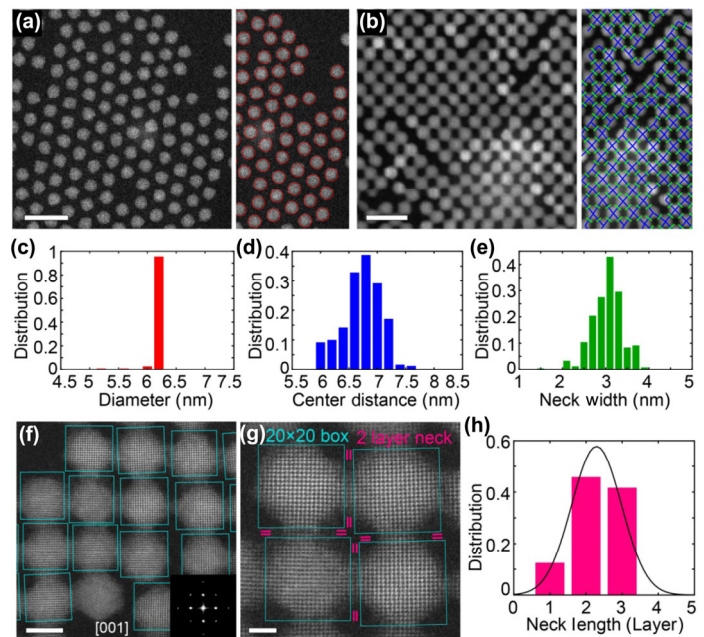


**Figure 3** *Ex situ* HAADF-STEM characterization of neck structure in large-area superlattices. (a) and (b) HAADF-STEM images of a hexagonal oleate-capped nanocrystal monolayer and an epitaxially-connected square superlattice. Right columns show the nanocrystal diameter (red circles), center-to-center distance (blue lines), and neck width (green lines) in half of each image as determined by computer vision (Fig. S3 in the ESM). (c) Histogram showing the distribution of nanocrystal diameter in the hexagonal monolayer in (a). (d) and (e) Histograms showing the distribution of center-to-center distance and neck width in the square superlattice in (b). (f) Atomic-resolution image and fast Fourier transform image (inset) showing the uniform oriented attachment and neck connectivity in the square superlattice. Cyan boxes with a size of  $20 \times 20$  Pb layers help to visualize the neck lengths. (g) Magnified image of several necks that are two Pb layers (0.6 nm) long. (h) Histogram of neck length obtained by counting the extra Pb layers between nanocrystals as indicated in (g). Scale bars are 20 nm in (a) and (b), 5 nm in (f), and 2 nm in (g).

We performed DFT calculations to test the hypothesis of ligand-enforced separation and better understand the necking mechanism. In order to reduce the calculation time while retaining the main structures of oleate ligands and PbSe nanocrystals, we simulated the structure with an oleic acid fragment (the alkyl tail after the alkene group omitted) sandwiched between the {001} facets of two rock salt PbSe crystals (Fig. 4(a)). With decreasing gap distance, the system energy first decreases and then increases as the ligand is sterically confined within the inter-nanocrystal gap. The system energy is minimized at a gap distance of 0.55–0.8 nm, in accord with the final gap distance observed with *in situ* and *ex situ* TEM imaging.

We further evaluate the critical nucleus size by adding pairs of Pb and Se atoms into the 0.6 nm gap (Fig. 4(c)). The energy change  $\Delta E = E_{\text{necked}} - (E_{\text{double-slab}} + n \times E_{\text{bulk}})$ . Note that, in reality, the atoms for forming neck are most likely from the edge or surface of nanocrystals, which have higher energy than that of bulk crystals. Therefore, the calculated  $\Delta E$  does not represent the energy barrier of neck formation directly, instead, it provides the relative energy comparison of the structures with different neck thickness, which is important to show the different stability of filaments and thick necks. As shown in Fig. 4(d), when adding the first 9 pairs of Pb and Se atoms,  $\Delta E$  generally increases with considerable fluctuations caused by surface energy change. Upon further addition of Pb and Se atoms,  $\Delta E$  decreases and the fluctuations cease, indicating the existence of an energy barrier and critical size for neck initiation and growth. The critical nucleus contains 9 pairs of Pb and Se atoms, which is two atoms long and  $3 \times 3$  atoms thick, i.e., 0.9 nm in width. We note that this size is consistent with the *in situ* observation of neck formation in Fig. 2.

We reported *in situ* observation of neck formation of semiconductor nanocrystals in liquid phase. We show that neck formation between PbSe nanocrystals occurs in three stages: (i) nanocrystals approach each other and stop at a distance of 0.6 nm, separated by a low coverage of residual oleate ligands; (ii) a stable neck nucleates after a period of transient atomic filament formation; (iii) the neck increases in width at a fixed length, supplied by surface atoms from neighboring facets. We provide basic kinetic data (e.g., initiation time) and critical spatial information (e.g., gap distance and critical nucleus size) that can only be obtained through *in situ* investigations. We confirm the neck size by the statistics of *ex situ* formed large-area superlattices with atomic precision. We also elucidate the initiation and growth mechanisms by DFT calculations. By revealing the necking phenomenon in unprecedented atomic detail, this study provides critical insights into how individual nanocrystals transform into

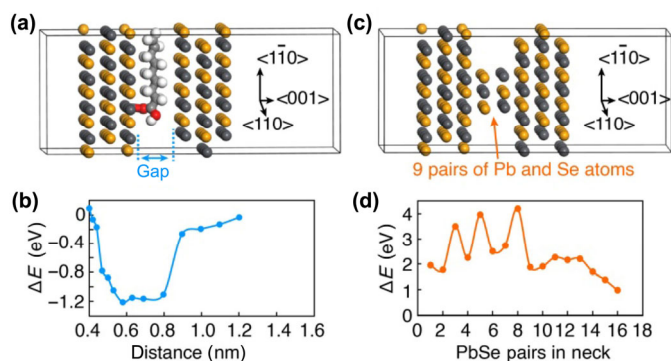


**Figure 4** DFT simulations of the inter-nanocrystal distance immediately prior to neck formation and the critical neck thickness during neck nucleation. (a) Sandwich structure with an oleic acid fragment between the {001} surfaces of two rock salt PbSe crystals. (b) The change of system energy as a function of gap distance. (c) Relaxed structure of two {001} surfaces with a neck consisting of nine pairs of Pb and Se atoms arranged in a  $3 \times 3 \times 2$  cuboid. (d)  $\Delta E$  changes as moving different pairs of Pb and Se atoms from bulk into the gap, showing the instability of thin filaments with few atom pairs and the increased stability of necks with more than 9 atom pairs.

epitaxially connected superlattices. Our improved understanding of neck initiation and growth will facilitate the fabrication of epitaxially-connected nanocrystal superlattices with better neck connectivity and uniformity, which may prove essential for achieving mini-band transport in these materials.

## Acknowledgements

This work was supported by the U.S. Department of Energy (DOE), Office of Science, Office of Basic Energy Sciences (BES), Materials Sciences and Engineering Division under Contract No. DE-AC02-05-CH11231 within the *in-situ* TEM (KC22ZH) program. Y. W., A. A., C. Q., and M. L. were supported by the UC Office of the President under the UC Laboratory Fees Research Program Collaborative Research and Training Award LFR-17-477148. X. P. acknowledges financial support from the China Scholarship Council. Work at the Molecular Foundry was supported by the Office of Science, Office of Basic Energy Sciences, of the U.S. Department of Energy under Contract No. DE-AC02-05CH11231.

**Electronic Supplementary Material:** Supplementary material (e.g., additional *in situ* movie analysis, STEM imaging, image processing method, and calculation method) is available in the online version of this article at <https://doi.org/10.1007/s12274-019-2483-8>.

## References

- Zhang, X.; Shen, Z.; Liu, J.; Kerisit, S. N.; Bowden, M. E.; Sushko, M. L.; De Yoreo, J. J.; Rosso, K. M. Direction-specific interaction forces underlying zinc oxide crystal growth by oriented attachment. *Nat. Commun.* **2017**, *8*, 835.
- Li, D. S.; Nielsen, M. H.; Lee, J. R. I.; Frandsen, C.; Banfield, J. F.; De Yoreo, J. J. Direction-specific interactions control crystal growth by oriented attachment. *Science* **2012**, *336*, 1014–1018.
- Whitham, K.; Smilgies, D. M.; Hanrath, T. Entropic, enthalpic, and kinetic aspects of interfacial nanocrystal superlattice assembly and attachment. *Chem. Mater.* **2018**, *30*, 54–63.
- Sandeep, C. S. S.; Azpiroz, J. M.; Evers, W. H.; Boehme, S. C.; Moreels, I.; Kinge, S.; Siebbeles, L. D. A.; Infante, I.; Houtepen, A. J. Epitaxially connected PbSe quantum-dot films: Controlled neck formation and optoelectronic properties. *ACS Nano* **2014**, *8*, 11499–11511.
- Lim, T. H.; McCarthy, D.; Hendy, S. C.; Stevens, K. J.; Brown, S. A.; Tilley, R. D. Real-time TEM and kinetic Monte Carlo studies of the coalescence of decahedral gold nanoparticles. *ACS Nano* **2009**, *3*, 3809–3813.
- Simon, P.; Bahrig, L.; Baburin, I. A.; Formanek, P.; Röder, F.; Sickmann, J.; Hickey, S. G.; Eychmuller, A.; Lichte, H.; Knip, R. et al. Interconnection of nanoparticles within 2D superlattices of PbS/oleic acid thin films. *Adv. Mater.* **2014**, *26*, 3042–3049.
- Whitham, K.; Hanrath, T. Formation of epitaxially connected quantum dot solids: Nucleation and coherent phase transition. *J. Phys. Chem. Lett.* **2017**, *8*, 2623–2628.
- Xu, Y. H.; Wang, X. X.; Zhang, W. L.; Lv, F.; Guo, S. J. Recent progress in two-dimensional inorganic quantum dots. *Chem. Soc. Rev.* **2018**, *47*, 586–625.
- Talpin, D. V.; Lee, J. S.; Kovalenko, M. V.; Shevchenko, E. V. Prospects of colloidal nanocrystals for electronic and optoelectronic applications. *Chem. Rev.* **2010**, *110*, 389–458.
- Boles, M. A.; Engel, M.; Talpin, D. V. Self-assembly of colloidal nanocrystals: From intricate structures to functional materials. *Chem. Rev.* **2016**, *116*, 11220–11289.
- Kagan, C. R.; Lifshitz, E.; Sargent, E. H.; Talpin, D. V. Building devices from colloidal quantum dots. *Science* **2016**, *353*, aac5523.
- Boneschanscher, M. P.; Evers, W. H.; Geuchies, J. J.; Altantzis, T.; Goris, B.; Rabouw, F. T.; van Rossum, S. A. P.; van der Zant, H. S. J.; Siebbeles, L. D. A.; van Tendeloo, G. et al. Long-range orientation and atomic attachment of nanocrystals in 2D honeycomb superlattices. *Science* **2014**, *344*, 1377–1380.
- Beugeling, W.; Kalesaki, E.; Delerue, C.; Niquet, Y. M.; Vanmaekelbergh, D.; Smith, C. M. Topological states in multi-orbital HgTe honeycomb lattices. *Nat. Commun.* **2015**, *6*, 6316.

- [14] Whitham, K.; Yang, J.; Savitzky, B. H.; Kourkoutis, L. F.; Wise, F.; Hanrath, T. Charge transport and localization in atomically coherent quantum dot solids. *Nat. Mater.* **2016**, *15*, 557–563.
- [15] Evers, W. H.; Schins, J. M.; Aerts, M.; Kulkarni, A.; Capiod, P.; Berthe, M.; Grandidier, B.; Delerue, C.; van der Zant, H. S. J.; van Overbeek, C. et al. High charge mobility in two-dimensional percolative networks of PbSe quantum dots connected by atomic bonds. *Nat. Commun.* **2015**, *6*, 8195.
- [16] Geuchies, J. J.; van Overbeek, C.; Evers, W. H.; Goris, B.; de Backer, A.; Gantapara, A. P.; Rabouw, F. T.; Hilhorst, J.; Peters, J. L.; Konovalov, O. et al. *In situ* study of the formation mechanism of two-dimensional superlattices from PbSe nanocrystals. *Nat. Mater.* **2016**, *15*, 1248–1254.
- [17] Weidman, M. C.; Smilgies, D. M.; Tisdale, W. A. Kinetics of the self-assembly of nanocrystal superlattices measured by real-time *in situ* X-ray scattering. *Nat. Mater.* **2016**, *15*, 775–781.
- [18] Zaluzhnyy, I. A.; Kurta, R. P.; Andre, A.; Gorobtsov, O. Y.; Rose, M.; Skopintsev, P.; Besedin, I.; Zozulya, A. V.; Sprung, M.; Schreiber, F. et al. Quantifying angular correlations between the atomic lattice and the superlattice of nanocrystals assembled with directional linking. *Nano Lett.* **2017**, *17*, 3511–3517.
- [19] Yalcin, A. O.; Fan, Z. C.; Goris, B.; Li, W. F.; Koster, R. S.; Fang, C. M.; van Blaaderen, A.; Casavola, M.; Tichelaar, F. D.; Bals, S. et al. Atomic resolution monitoring of cation exchange in CdSe-PbSe heteronanocrystals during epitaxial solid-solid-vapor growth. *Nano Lett.* **2014**, *14*, 3661–3667.
- [20] Cho, K. S.; Talapin, D. V.; Gaschler, W.; Murray, C. B. Designing PbSe nanowires and nanorings through oriented attachment of nanoparticles. *J. Am. Chem. Soc.* **2005**, *127*, 7140–7147.
- [21] Evers, W. H.; Goris, B.; Bals, S.; Casavola, M.; de Graaf, J.; van Roij, J.; Dijkstra, M.; Vanmaekelbergh, D. Low-dimensional semiconductor superlattices formed by geometric control over nanocrystal attachment. *Nano Lett.* **2013**, *13*, 2317–2323.
- [22] van Overbeek, C.; Peters, J. L.; van Rossum, S. A. P.; Smits, M.; van Huis, M. A.; Vanmaekelbergh, D. Interfacial self-assembly and oriented attachment in the family of PbX (X = S, Se, Te) nanocrystals. *J. Phys. Chem. C* **2018**, *122*, 12464–12473.
- [23] Tan, S. F.; Chee, S. W.; Lin, G. H.; Mirsaidov, U. Direct observation of interactions between nanoparticles and nanoparticle self-assembly in solution. *Acc. Chem. Res.* **2017**, *50*, 1303–1312.
- [24] Qi, K.; Wei, J. K.; Sun, M. H.; Huang, Q. M.; Li, X. M.; Xu, Z.; Wang, W. L.; Bai, X. D. Real-time observation of deep lithiation of tungsten oxide nanowires by *in situ* electron microscopy. *Angew. Chem., Int. Ed.* **2015**, *127*, 15437–15440.
- [25] Wu, S. Y.; Li, M. R.; Sun, Y. G. *In situ* synchrotron X-ray characterization shining light on the nucleation and growth kinetics of colloidal nanoparticles. *Angew. Chem., Int. Ed.* **2019**, *58*, 8987–8995.
- [26] Kim, J.; Ou, Z. H.; Jones, M. R.; Song, X. H.; Chen, Q. Imaging the polymerization of multivalent nanoparticles in solution. *Nat. Commun.* **2017**, *8*, 761.
- [27] de Yoreo, J. J.; Gilbert, P. U. P. A.; Sommerdijk, N. A. J. M.; Penn, R. L.; Whitlam, S.; Joester, D.; Zhang, H. Z.; Rimer, J. D.; Navrotsky, A.; Banfield, J. F. et al. Crystallization by particle attachment in synthetic, biogenic, and geologic environments. *Science* **2015**, *349*, aaa6760.
- [28] Urban, J. J. Prospects for thermoelectricity in quantum dot hybrid arrays. *Nat. Nanotechnol.* **2015**, *10*, 997–1001.
- [29] Liao, H. G.; Zheng, H. Liquid cell transmission electron microscopy. *Annu. Rev. Phys. Chem.* **2016**, *67*, 719–747.
- [30] Yuan, W. T.; Zhang, D. W.; Ou, Y.; Fang, K.; Zhu, B. E.; Yang, H. S.; Hansen, T. W.; Wagner, J. B.; Zhang, Z.; Gao, Y. et al. Direct *in situ* TEM visualization and insight into the facet-dependent sintering behaviors of gold on TiO<sub>2</sub>. *Angew. Chem., Int. Ed.* **2018**, *57*, 16827–16831.
- [31] Sutter, E.; Sutter, P.; Tkachenko, A. V.; Krahn, R.; de Graaf, J.; Arciniegas, M.; Manna, L. *In situ* microscopy of the self-assembly of branched nanocrystals in solution. *Nat. Commun.* **2016**, *7*, 11213.
- [32] Kim, B. H.; Yang, J.; Lee, D.; Choi, B. K.; Hyeon, T.; Park, J. Liquid-phase transmission electron microscopy for studying colloidal inorganic nanoparticles. *Adv. Mater.* **2018**, *30*, 1703316.
- [33] Wang, Y.; Peng, X. X.; Abelson, A.; Xiao, P. H.; Qian, C.; Yu, L.; Ophus, C.; Ercius, P.; Wang, L. W.; Law, M. et al. Dynamic deformability of individual PbSe nanocrystals during superlattice phase transitions. *Sci. Adv.* **2019**, *5*, eaaw5623.
- [34] Klokkenburg, M.; Houtepen, A. J.; Koole, R.; de Folter, J. W. J.; Ern , B. H.; van Faassen, E.; Vanmaekelbergh, D. Dipolar structures in colloidal dispersions of PbSe and CdSe quantum dots. *Nano Lett.* **2007**, *7*, 2931–2936.
- [35] Yuk, J. M.; Park, J.; Ercius, P.; Kim, K.; Hellebusch, D. J.; Crommie, M. F.; Lee, J. Y.; Zettl, A.; Alivisatos, A. P. High-resolution em of colloidal nanocrystal growth using graphene liquid cells. *Science* **2012**, *336*, 61–64.
- [36] Jin, B.; Sushko, M. L.; Liu, Z. M.; Jin, C. H.; Tang, R. K. *In situ* liquid cell tem reveals bridge-induced contact and fusion of Au nanocrystals in aqueous solution. *Nano Lett.* **2018**, *18*, 6551–6556.
- [37] Anand, U.; Lu, J. Y.; Loh, D.; Aabdin, Z.; Mirsaidov, U. Hydration layer-mediated pairwise interaction of nanoparticles. *Nano Lett.* **2016**, *16*, 786–790.
- [38] Zhu, C.; Liang, S. X.; Song, E. H.; Zhou, Y. J.; Wang, W.; Shan, F.; Shi, Y. T.; Hao, C.; Yin, K. B.; Zhang, T. et al. *In-situ* liquid cell transmission electron microscopy investigation on oriented attachment of gold nanoparticles. *Nat. Commun.* **2018**, *9*, 421.
- [39] Anderson, N. C.; Hendricks, M. P.; Choi, J. J.; Owen, J. S. Ligand exchange and the stoichiometry of metal chalcogenide nanocrystals: Spectroscopic observation of facile metal-carboxylate displacement and binding. *J. Am. Chem. Soc.* **2013**, *135*, 18536–18548.